Linear and nonlinear spin-current generation in polar collinear antiferromagnets without relativistic spin-orbit coupling

Satoru Hayami
Graduate School of Science, Hokkaido University, Sapporo 060-0810, Japan

(Received 7 April 2024; revised 4 June 2024; accepted 10 June 2024; published 21 June 2024)

We investigate spin-current generation in polar collinear antiferromagnets without relying on the relativistic spin-orbit coupling. The symmetry and microscopic model analyses indicate that both linear and nonlinear spin conductivities are induced; the linear spin conductivity is characterized by the non-Hall-type transverse tensor component, while the nonlinear spin conductivity is characterized by the Hall-type tensor component. We show that the emergence of the linear and nonlinear spin currents is caused by the quadrupole and dipole components of the magnetic toroidal multipoles in the collinear antiferromagnetic structure, respectively. We demonstrate the important conditions to enhance and/or suppress the spin conductivity in each component by analyzing a fundamental tight-binding model. The experimental separation between their contributions is also discussed.

DOI: 10.1103/PhysRevB.109.214431

I. INTRODUCTION

Relativistic spin-orbit coupling (SOC) has been the subject of considerable interest in both theory and experiments in condensed-matter physics, since it brings about intriguing quantum states of matter and physical phenomena, such as the topological insulator [1,2], topological magnetism [3–5], the spin Hall effect [6,7], multiferroics [8–11], the anomalous Hall effect [12–16], nonreciprocal transport [17–19], and noncentrosymmetric superconductivity [20–22]. Meanwhile, the flexible control of the SOC is difficult, since its effective magnitude in solids is intrinsically determined by lattice structures and constituent elements.

Recently, it was shown that such SOC-related phenomena have been achieved by considering a certain type of antiferromagnets (AFMs) even without the SOC. One of the typical examples is the spin-current generation that originates from the symmetric momentum-dependent spin splitting in the electronic band structure under collinear AFMs [23–47]. Since the appearance of the momentum-dependent spin polarization requires neither net magnetization nor SOC, it can be expected by a high-efficient spin-current generator [26,31,34,48,49]. The conditions causing the SOC-free spin-split band structure have been clarified based on the symmetry analysis by using magnetic point group theory [33,50], spin group theory [51–54], and magnetic layer group theory [55] and microscopic analysis based on electronic multipole moments [27,29,34]. Furthermore, such a concept has been extended so as to include noncollinear and noncoplanar AFMs with the breaking of the spatial inversion symmetry; the noncollinear AFM leads to the antisymmetric spin-split band structure like the Rashba-type spin splitting [29,56,57], while the noncoplanar AFM leads to the asymmetric band modulation resulting in the nonreciprocal transport [58–62].

In the present study, we further investigate physical phenomena in such SOC-free AFMs. Among them, we analyze the spin-current generation in collinear AFMs under the polar crystal structure by focusing on the role of spatial inversion symmetry breaking. Although the breaking of the spatial inversion symmetry does not cause a further antisymmetric spin splitting, as found in noncollinear AFMs, owing to the spin rotational symmetry in collinear AFM structures [27], we show that nonlinear spin transport is induced without relying on the spin-split band structure in addition to the linear spin transport. We clarify that a nonzero linear (nonlinear) spin conductivity is obtained when the collinear AFM structure accompanies the cluster magnetic toroidal quadrupole (magnetic toroidal dipole) through symmetry and microscopic model analyses [34,63]. We also show the microscopic conditions to enhance and suppress either the linear or nonlinear spin conductivity. The present results can apply to not only polar crystal systems but also surface systems, the latter of which often appears in the situation when one tries to engineer quasi-two-dimensional spintronics devices from three-dimensional centrosymmetric collinear AFMs.

The rest of this paper is organized as follows. In Sec. II, we discuss the symmetry conditions needed to exhibit both linear and nonlinear spin conductivities in polar collinear AFMs based on the multipole representation. In Sec. III, we introduce a minimal tight-binding model and AFM structures accompanying both dipole and quadrupole components in the magnetic toroidal multipole. In Sec. IV, we show the calculation results in terms of the electronic band structure, the linear spin conductivity, and the nonlinear spin conductivity. We discuss the similar and different tendencies between linear and nonlinear spin conductivities in Sec. V. Section VI is devoted to a summary of the paper.

II. SYMMETRY ANALYSIS

In this section, we briefly introduce the correspondence between linear and nonlinear spin conductivities and the multipoles under the polar magnetic point group [50,64] rather than the spin group [51–54,65–67] with the materials to have

a small but non-negligible SOC in mind. The linear and nonlinear spin conductivity tensors are defined by

$$J_{\nu}^{\eta(\mathrm{s})} = \sum_{\mu} \sigma_{\mu\nu}^{\eta(\mathrm{s})} E_{\mu}, \tag{1}$$

$$J_{\gamma}^{\eta(\mathrm{s})} = \sum_{\mu\nu} \sigma_{\gamma\mu\nu}^{\eta(\mathrm{s})} E_{\mu} E_{\nu}, \tag{2}$$

where $J_{\nu}^{\eta(\mathrm{s})} = J_{\nu}\sigma_{\eta}$ represents the spin current with the spin σ_{η} for the $\eta = x, y, z$ component and E_{μ} represents the electric field for the $\mu = x, y, z$ direction; $\nu, \gamma = x, y, z$. The spin component in the spin current is parallel to the AFM moment direction owing to the collinear AFM structure without the SOC. The symmetric component of the linear spin conductivity tensor, i.e., $\sigma_{\mu\nu}^{\eta(\mathrm{s})} = \sigma_{\nu\mu}^{\eta(\mathrm{s})}$, and the Hall-type antisymmetric component of the nonlinear spin conductive tensor with $\sigma_{\gamma\mu\nu}^{\eta(\mathrm{s})} = \sigma_{\gamma\nu\mu}^{\eta(\mathrm{s})}$ can be induced depending on the magnetic symmetry.

Microscopically, the linear spin conductivity is caused by the quadrupole-type spin-split band structure in terms of the wave vector under the collinear AFM structure [26]; the functional form of the spin splitting in momentum space is generally given by $k_{\mu}k_{\nu}\sigma_{\eta}$ in the $\boldsymbol{k} \to \boldsymbol{0}$ limit, which indicates that the spin current with the same symmetry as $k_{\nu}\sigma_{\eta}$ ($k_{\mu}\sigma_{\eta}$) is induced by applying the electric current with the same symmetry as k_{μ} (k_{ν}) driven by the electric field along the μ (ν) direction. In other words, the spin splitting in the form of $k_{\mu}k_{\nu}\sigma_{\eta}$ naturally induces nonzero $\sigma_{\mu\nu}^{\eta(\mathrm{s})}$. The nonzero component in $\sigma_{\mu\nu}^{\eta(\mathrm{s})}$ is determined by the crystal symmetry, which is classified based on group theory [50,68–70]. It is noted that the breaking of the spatial inversion symmetry is not necessary in inducing the linear spin conductivity.

In order to systematically describe the appearance of the quadrupole-type symmetric spin-split band structure in collinear AFMs, we introduce the concept of the complete multipole representation, which consists of four types of multipoles: electric multipoles (Q_{lm}) describing the time-reversal-even polar tensor quantity, electric toroidal multipoles (G_{lm}) describing the time-reversal-even axial tensor quantity, magnetic multipoles (M_{lm}) describing the time-reversal-odd axial tensor quantity, and magnetic toroidal multipoles (T_{lm}) describing the time-reversal-odd polar tensor quantity [71]; the subscripts of multipoles represent the rank l and its component m. Since four types of multipoles constitute a complete set in physical Hilbert space, one can express any physical quantities in both real and momentum spaces as a linear combination of the above multipoles.

By using the multipole representation, the quadrupole-type spin splitting $k_{\mu}k_{\nu}\sigma_{\eta}$ is described by the magnetic toroidal quadrupoles $T_{2m} = (T_u, T_v, T_{yz}, T_{zx}, T_{xy})$, which are characterized by the functional form of $(3z^2 - r^2, x^2 - y^2, yz, zx, xy)$, respectively, and the magnetic octupoles $M_{3m} = (M_{xyz}, M_x^{\alpha}, M_y^{\alpha}, M_z^{\alpha}, M_x^{\beta}, M_y^{\beta}, M_z^{\beta})$, which are characterized by the functional forms of $[xyz, x(5x^2 - 3r^2), y(5y^2 - 3r^2), z(5z^2 - 3r^2), x(y^2 - z^2), y(z^2 - x^2), z(x^2 - y^2)]$, respectively [50]. We show the correspondence between the symmetric spin-split band dispersion and multipoles in Table I. One finds that a variety of the symmetric spin-split band dispersions occur when any of T_{2m} and M_{3m} belong to the totally symmetric irreducible representation under targeting magnetic point groups. For example, in the case of T_v, the k_yk_z-type spin splitting is expected when the AFM moment lies along the x direction, while the k_xk_y-type spin splitting is expected when the AFM moment lies along the z direction. As is discussed in Sec. III, T_{2m} and M_{3m} correspond to the macroscopic AFM order parameter based on the cluster multipole theory [72–75].

TABLE I. Relationship between the symmetric spin-split band structures and multipoles according to the different components of the spin polarization $(\sigma_x, \sigma_y, \sigma_z)$. $(T_u, T_v, T_{yz}, T_{zx}, T_{xy})$ represent the magnetic toroidal quadrupole and $(M_{xyz}, M_x^{\alpha}, M_y^{\alpha}, M_z^{\alpha}, M_x^{\beta}, M_y^{\beta}, M_z^{\beta})$ represent the magnetic octupole. $k^2 = k_x^2 + k_y^2 + k_z^2$.

	σ_x	σ_y	σ_z
T_u	$-k_yk_z$	k_zk_x	—
T_v	$-k_yk_z$	$-k_zk_x$	$2k_xk_y$
T_{yz}	$-(k_y^2 - k_z^2)$	k_xk_y	$-k_zk_x$
T_{zx}	$-k_xk_y$	$-(k_z^2 - k_x^2)$	k_yk_z
T_{xy}	k_zk_x	$-k_yk_z$	$-(k_x^2 - k_y^2)$
M_{xyz}	k_yk_z	k_zk_x	k_xk_y
M_x^{α}	$\frac{1}{2}(3k_x^2 - k^2)$	$-k_xk_y$	$-k_zk_x$
M_y^{α}	$-k_xk_y$	$\frac{1}{2}(3k_y^2 - k^2)$	$-k_yk_z$
M_z^{α}	$-k_zk_x$	$-k_yk_z$	$\frac{1}{2}(3k_z^2 - k^2)$
M_x^{β}	$-k_xk_y$	k_xk_y	k_yk_z
M_y^{β}	$\frac{1}{2}(k_y^2 - k_z^2)$	$\frac{1}{2}(k_z^2 - k_x^2)$	$-k_zk_x$
M_z^{β}	k_zk_x	$-k_yk_z$	$\frac{1}{2}(k_x^2 - k_y^2)$

In contrast to $\sigma_{\mu\nu}^{\eta(\mathrm{s})}$, the spatial inversion symmetry breaking is required for obtaining nonzero nonlinear spin Hall conductivity $\sigma_{\gamma\mu\nu}^{\eta(\mathrm{s})}$ [76–80]. From the multipole viewpoint, the rank-1 magnetic toroidal dipoles $T_{1m} = (T_x, T_y, T_z)$ and rank-2 magnetic quadrupoles $M_{2m} = (M_u, M_v, M_{yz}, M_{zx}, M_{xy})$ with spatial inversion odd contribute to $\sigma_{\gamma\mu\nu}^{\eta(\mathrm{s})}$ when the spin-dependent Berry curvature dipole mechanism is considered; the correspondence between multipoles and the tensor components has been discussed in Ref. [63]. It is noted that the spin-split band structure is not essentially necessary in inducing the nonlinear spin conductivity, since the multipoles T_{1m} and M_{2m} preserve the product symmetry of the spatial inversion and time-reversal operations.

The above discussions indicate that the linear spin conductivity is induced when any of the magnetic toroidal quadrupoles and magnetic octupoles belong to the totally symmetric irreducible representation under the magnetic point group, while the nonlinear spin Hall conductivity is induced when any of the magnetic toroidal dipoles and magnetic quadrupoles belong to the totally symmetric irreducible representation. Since all the multipoles are systematically classified under 122 magnetic point groups [64], one finds which magnetic point groups can exhibit both linear and nonlinear spin conductivities.

One of the candidate situations to exhibit both linear and nonlinear spin conductivities is that the electric field is applied to collinear AFMs with the magnetic toroidal quadrupole and/or magnetic octupole so that the inversion symmetry is lost. We consider such a symmetry situation in the following analysis. There are 21 magnetic point groups with keeping polar symmetry. We show the active relevant multipoles under

TABLE II. Active multipoles under 21 polar magnetic point groups without the time-reversal symmetry. $T_{2m} = (T_u, T_v, T_{yz}, T_{zx}, T_{xy})$ and $M_{3m} = (M_{xyz}, M_x^\alpha, M_y^\alpha, M_z^\alpha, M_x^\beta, M_y^\beta, M_z^\beta)$ represent the magnetic toroidal quadrupole and the magnetic octupole with the spatial inversion even, respectively, and $T_{1m} = (T_x, T_y, T_z)$ and $M_{2m} = (M_u, M_v, M_{yz}, M_{zx}, M_{xy})$ represent the magnetic toroidal dipole and the magnetic quadrupole with spatial inversion odd, respectively; $M_{3a} = (\sqrt{10}M_x^\alpha - \sqrt{6}M_x^\beta)/4$ and $M_{3b} = -(\sqrt{10}M_y^\alpha + \sqrt{6}M_y^\beta)/4$. The emergence of (T_{2m}, M_{3m}) results in the linear spin conductivity originating from the symmetric spin-split band structure, while that of (T_{1m}, M_{2m}) results in the nonlinear spin Hall conductivity. The magnetic point groups with the ferromagnetic moment, i.e., the magnetic dipole M_{1m}, are also shown for reference.

MPG	T_{2m}	M_{3m}	T_{1m}	M_{2m}	M_{1m}
1	$T_u, T_v, T_{yz}, T_{zx}, T_{xy}$	$M_{xyz}, M_x^\alpha, M_y^\alpha, M_z^\alpha, M_x^\beta, M_y^\beta, M_z^\beta$	T_x, T_y, T_z	$M_u, M_v, M_{yz}, M_{zx}, M_{xy}$	M_x, M_y, M_z
2	T_u, T_v, T_{zx}	$M_{xyz}, M_y^\alpha, M_y^\beta$	T_y	M_u, M_v, M_{zx}	M_y
3	T_u	$M_z^\alpha, M_{3a}, M_{3b}$	T_z	M_u	M_z
4, 6	T_u	M_z^α	T_z	M_u	M_z
$2'$	T_{yz}, T_{xy}	$M_x^\alpha, M_z^\alpha, M_x^\beta, M_z^\beta$	T_x, T_z	M_{yz}, M_{xy}	M_x, M_z
$4'$	T_v, T_{xy}	M_{xyz}, M_z^β	—	M_v, M_{xy}	—
$6'$	—	M_{3a}, M_{3b}	—	—	—
m	T_u, T_v, T_{zx}	$M_{xyz}, M_y^\alpha, M_y^\beta$	T_x, T_z	M_{yz}, M_{xy}	M_y
m'	T_{yz}, T_{xy}	$M_x^\alpha, M_z^\alpha, M_x^\beta, M_z^\beta$	T_y	M_u, M_v, M_{zx}	M_x, M_z
$mm2$	T_u, T_v	M_{xyz}	T_z	M_{xy}	—
$3m$	T_u	M_{3b}	T_z	—	—
$4mm, 6mm$	T_u	—	T_z	—	—
$m'm'2$	T_{xy}	M_z^α, M_z^β	—	M_u, M_v	M_z
$3m'$	—	M_z^α, M_{3a}	—	M_u	M_z
$4m'm', 6m'm'$	—	M_z^α	—	M_u	M_z
$m'm2'$	T_{zx}	M_y^α, M_y^β	T_x	M_{yz}	M_y
$4'mm'$	T_v	M_{xyz}	—	M_{xy}	—
$6'mm'$	—	M_{3b}	—	—	—

such polar magnetic point groups without the time-reversal symmetry in Table II. In each magnetic point group, one expects the appearance of the linear and/or nonlinear spin conductivities according to the different types of active multipoles. For example, in the case of $mm2$, the functional form of the symmetric spin splitting is given by $c_1 k_y k_z \sigma_x + c_2 k_z k_x \sigma_y + c_3 k_x k_y \sigma_z$ with the coefficients c_1, c_2, and c_3 owing to active T_u, T_v, and M_{xyz}. Then, we expect nonzero tensor components of the linear spin conductivity $\sigma_{yz}^{x(\mathrm{s})} = \sigma_{zy}^{x(\mathrm{s})}$ for the collinear AFM with the x-spin polarization. In addition, nonzero tensor components of the nonlinear spin Hall conductivity $\sigma_{yxx}^{x(\mathrm{s})} = -2\sigma_{xyx}^{x(\mathrm{s})}$ and $\sigma_{yzz}^{x(\mathrm{s})} = -2\sigma_{zyz}^{x(\mathrm{s})}$ appear owing to active T_z.

III. MODEL

In order to analyze the difference between linear and nonlinear spin conductivities from the microscopic point of view, we investigate a minimal tight-binding model. We consider a four-sublattice system under the two-dimensional tetragonal lattice structure with the magnetic point group $4/mmm1'$, as shown in Fig. 1(a); the positions of the four sublattice sites A–D are given by $\boldsymbol{r}_\mathrm{A} = (-1/2, -1/2)a$, $\boldsymbol{r}_\mathrm{B} = (1/2, 1/2)a$, $\boldsymbol{r}_\mathrm{C} = (1/2, -1/2)a$, and $\boldsymbol{r}_\mathrm{D} = (-1/2, 1/2)a$, with $a = b = 0.5$. Supposing the single s-orbital degree of freedom at each lattice site, the tight-binding model is given by

$$\mathcal{H}^\mathrm{T} = -\sum_{\boldsymbol{k}\sigma}\sum_{ij} t_{ij} c_{\boldsymbol{k}i\sigma}^\dagger c_{\boldsymbol{k}j\sigma} - h_\mathrm{AFM}\sum_{\boldsymbol{k}i\sigma} p_i(\sigma) c_{\boldsymbol{k}i\sigma}^\dagger c_{\boldsymbol{k}i\sigma}, \quad (3)$$

where $c_{\boldsymbol{k}i\sigma}^\dagger$ ($c_{\boldsymbol{k}i\sigma}$) is the creation (annihilation) operator at wave vector $\boldsymbol{k}$, sublattice i, and spin σ. The first term represents the hopping between different sublattices. We consider four hopping parameters: the two intraplaquette hoppings $t_a = 1$ and $t_a' = 0.3$ and the two interplaquette hoppings $t_b = 0.9$

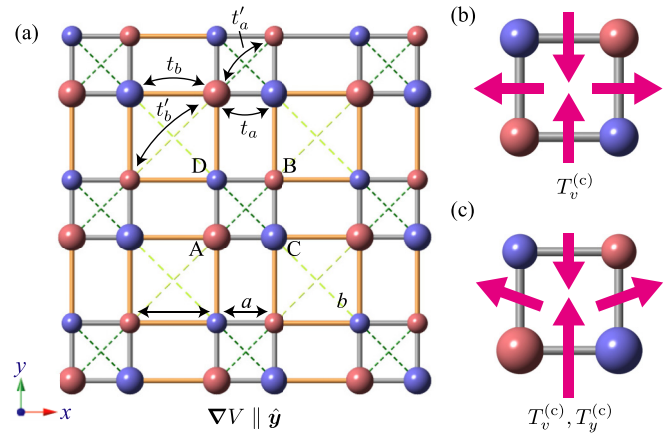

FIG. 1. (a) Two-dimensional tetragonal crystal structure with four sublattices A–D. The red and blue spheres represent the spin polarization along the $+z$ and $-z$ directions, respectively. The magnitude of the spheres represents that of the charge density, which leads to the potential gradient along the y direction ($\nabla V \parallel \hat{\boldsymbol{y}}$) and makes the system polar. (b), (c) Spatial distributions of the magnetic toroidal dipoles on each bond denoted by the magenta arrows for the four-sublattice plaquette (b) without the charge-density modulation and (c) with the charge-density modulation. The situation in panel (b) corresponds to the appearance of the cluster magnetic toroidal quadrupole $T_v^{(\mathrm{c})}$, while that in panel (c) corresponds to the appearance of the cluster magnetic toroidal dipole $T_y^{(\mathrm{c})}$ in addition to $T_v^{(\mathrm{c})}$.

and $t_b' = 0.27$ [see Fig. 1(a)]; t_a is taken as the energy unit of the model. The other choices of the hopping parameters do not affect the following results qualitatively. The second term represents the molecular field causing the collinear AFM structure; $h_{\rm AFM}$ represents the magnitude of the molecular field and $p_{\rm A,B}(\sigma) = +1(-1)$ and $p_{\rm C,D}(\sigma) = -1(+1)$ represents the up(down)-spin $\sigma = +1$ ($\sigma = -1$) component, whose configuration is schematically presented in Fig. 1(a). Although the direction of the spin moments is arbitrarily taken owing to the spin rotational symmetry without the SOC, we set the quantization axis along the z direction for simplicity. In the presence of nonzero $h_{\rm AFM}$, the symmetry of the system reduces from $4/mmm1'$ to $4'/mmm'$.

In addition to the above Hamiltonian, we take into account the polar crystalline electric field in order to discuss the effect of the spatial inversion symmetry breaking. For that purpose, we consider the following symmetry-lowering term

$$\mathcal{H}^{\rm CO} = -h_{\rm CO} \sum_{\boldsymbol{k}i\sigma} q_i c^\dagger_{\boldsymbol{k}i\sigma} c_{\boldsymbol{k}i\sigma}, \tag{4}$$

where $q_{\rm A} = q_{\rm C} = 1$ and $q_{\rm B} = q_{\rm D} = -1$. This term corresponds to the charge-density modulation when the polar electric field (potential gradient) along the y direction exists. Nonzero $h_{\rm CO}$ leads to further symmetry lowering from $4'/mmm'$ to $m2m$, where the twofold rotational axis remains along the y direction.

We discuss the corresponding multipole moments under nonzero $h_{\rm AFM}$ and $h_{\rm CO}$ based on the cluster multipole theory [72–75]. For $h_{\rm AFM} \neq 0$ and $h_{\rm CO} = 0$, the four-sublattice collinear AFM structure holds the symmetry combined with the fourfold rotation and time-reversal operations, as shown by the square plaquette in Fig. 1(b). When calculating the magnetic toroidal dipole moment on each bond within the square plaquette, which is defined as $\boldsymbol{t}_{ij} = \boldsymbol{r}_i \times \boldsymbol{s}_i + \boldsymbol{r}_j \times \boldsymbol{s}_j$ for the ij bond ($\boldsymbol{s}_i$ is the expectation value of the local spin moment at site i), one obtains

$$\boldsymbol{t}_{\rm AC} = (0, s, 0), \tag{5}$$

$$\boldsymbol{t}_{\rm BD} = (0, -s, 0), \tag{6}$$

$$\boldsymbol{t}_{\rm AD} = (-s, 0, 0), \tag{7}$$

$$\boldsymbol{t}_{\rm BC} = (s, 0, 0), \tag{8}$$

where we set $\boldsymbol{s}_{\rm A} = \boldsymbol{s}_{\rm B} = (0, 0, 2s)$ and $\boldsymbol{s}_{\rm C} = \boldsymbol{s}_{\rm D} = (0, 0, -2s)$ for notational simplicity. Thus, the magnetic toroidal dipole on the bond is spatially distributed in the x^2-y^2-type quadrupole form of $t^x_{ij} b^x_{ij} - t^y_{ij} b^y_{ij}$, where $\boldsymbol{b}_{ij} = (\boldsymbol{r}_i + \boldsymbol{r}_j)/2 = (b^x_{ij}, b^y_{ij}, b^z_{ij})$ represents the bond center vector for the ij bond [81–92]. In other words, the collinear AFM structure induced by $h_{\rm AFM}$ accompanies the cluster magnetic toroidal quadrupole $T_v^{\rm (c)}$; the superscript (c) denotes the cluster. It is noted that there is no uniform component in the magnetic toroidal moment, i.e., $\sum_{ij} \boldsymbol{t}_{ij} = \boldsymbol{0}$ for the four bonds AB, BC, CD, and DA; no dipole component appears.

Then, we further consider the situation for $h_{\rm CO} \neq 0$ in addition to $h_{\rm AFM} \neq 0$, whose spin and charge distributions within the square plaquette are shown in Fig. 1(c). Reflecting on the inequivalence between the A and B (C and D) sublattices, the uniform component of $\boldsymbol{t}_{ij}$ is induced in the positive y direction, as shown in Fig. 1(c). This result indicates that the cluster magnetic toroidal dipole $T_y^{\rm (c)}$ is additionally induced according to the symmetry lowering by the effective polar field $h_{\rm CO}$. Indeed, both the magnetic toroidal quadrupole $T_v^{\rm (c)}$ and the magnetic toroidal dipole $T_y^{\rm (c)}$ belong to the totally symmetric irreducible representation under the magnetic point group $m2m$ [64].

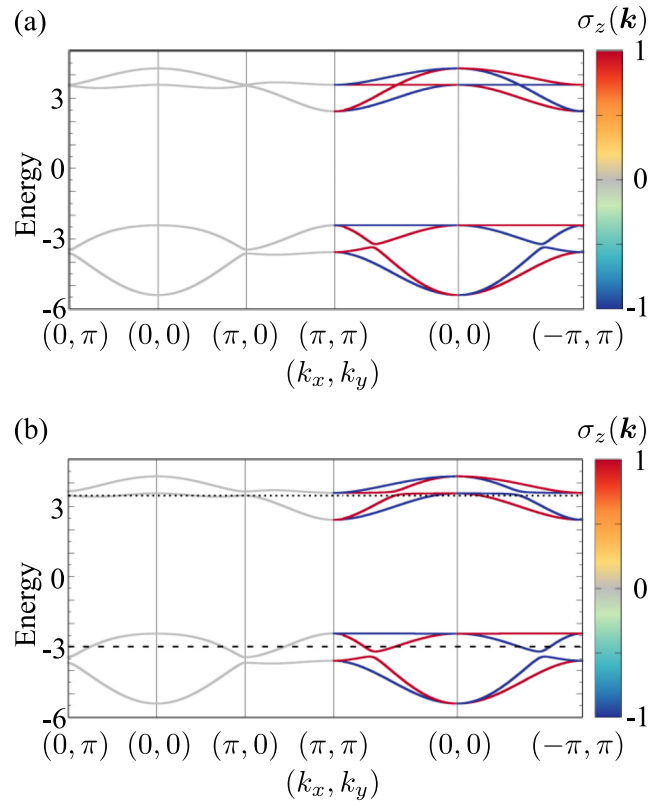

FIG. 2. Electronic band structure along the high-symmetric lines in the first Brillouin zone at (a) $h_{\rm CO} = 0$ and (b) $h_{\rm CO} = 0.1$ for $h_{\rm AFM} = 3$. The contour shows the z-spin polarization at each wave vector (k_x, k_y). In panel (b), the dashed (dotted) lines represent the energy where the absolute value of the linear (nonlinear) spin conductivity becomes maximum.

IV. RESULTS

We discuss the behavior of the linear and nonlinear spin conductivities under the polar collinear AFM without the SOC. First, we show the electronic band structure under the collinear AFM structure in Sec. IV A, where the symmetric spin-split band structure emerges. Then, we show the results of the linear and nonlinear spin conductivities in Secs. IV B and IV C, respectively.

A. Electronic band structure

Figure 2(a) shows the electronic band structure along the high-symmetric lines in the Brillouin zone at $h_{\rm CO} = 0$ and $h_{\rm AFM} = 3$, where only the cluster magnetic toroidal quadrupole $T_v^{\rm (c)}$ exists. In Fig. 2(a), the spin-split

band structure appears in the (π,π)–$(0,0)$–$(-\pi,\pi)$ line for (k_x,k_y), while no spin splitting occurs in the $(0,\pi)$–$(0,0)$–$(\pi,0)$ line. This indicates the emergence of the symmetric spin splitting in the form of $k_xk_y\sigma_z$, which is consistent with the symmetry argument in Sec. II.

When the effect of $h_{\rm CO}=0.1$ is introduced so that the magnetic toroidal dipole $T_y^{(\rm c)}$ is induced, the band dispersion also exhibits the symmetric spin splitting, as shown in Fig. 2(b). Compared to the result in Fig. 2(a), almost the same feature appears, which indicates that additional $T_y^{(\rm c)}$ does not affect the spin splitting.

The emergence of the symmetric spin splitting in the band structure depends on the model parameters. In the present total Hamiltonian $\mathcal{H}^{\rm T}+\mathcal{H}^{\rm CO}$, the symmetric spin splitting vanishes when the diagonal hoppings t_a' and t_b' are turned off despite the same magnetic symmetry. This is understood from the fact that only the diagonal hopping includes the momentum dependence corresponding to the same irreducible representation as the mean-field term, which results in an effective coupling between hoppings and AFM molecular fields, and hence, it is a source of the microscopic origin of the symmetric spin-split band structure [27]. Among the hoppings, only the diagonal hopping includes the functional form of k_xk_y in terms of the wave vector. Since such momentum dependence of k_xk_y has the same symmetry as the spatial distribution of the AFM molecular field, both of which belong to the B_{2g} representation under the magnetic point group $4/mmm1'$, the effective coupling between them can occur under the AFM ordering. In this way, the type of hoppings is important in inducing the symmetric spin splitting in the form of $k_xk_y\sigma_z$.

B. Linear spin conductivity

We examine the linear spin conductivity in Eq. (1) in the model Hamiltonian $\mathcal{H}^{\rm T}+\mathcal{H}^{\rm CO}$ based on the linear response theory. We calculate $\sigma_{\mu\nu}^{\eta({\rm s})}$ by evaluating the $J_\nu^{\eta({\rm s})}$–J_μ correlation function within the Kubo formula following Refs. [34,70] with the scattering rate $\tau^{-1}=10^{-2}$ and the temperature $T=10^{-2}$; the unit of T is Kelvin. The summation of the wave vector $\boldsymbol{k}$ is taken over $N_{\boldsymbol{k}}=2400^2$ grid points in the first Brillouin zone. For the collinear AFM structure in Fig. 1(a), nonzero tensor components are given by $\sigma_{xy}^{z({\rm s})}=\sigma_{yx}^{z({\rm s})}$ owing to the active magnetic toroidal quadrupole $T_v^{(\rm c)}$, as discussed in Sec. II; it is noted that the symmetric nature of the linear spin conductivity tensor is different from the antisymmetric nature of the spin Hall conductivity tensor.

Figure 3(a) shows the electron filling per site $n_e=\sum_{\boldsymbol{k}i\sigma}\langle c_{\boldsymbol{k}i\sigma}^\dagger c_{\boldsymbol{k}i\sigma}\rangle/(4N_{\boldsymbol{k}})$ and $h_{\rm CO}$ dependence of $\sigma_{xy}^{z({\rm s})}$ at $h_{\rm AFM}=3$. All the regions except for $n_e=0$ and 2 exhibit nonzero $\sigma_{xy}^{z({\rm s})}$, although its behavior in terms of the sign and magnitude is complicated, which might be attributed to the multiband structure. The intraband process proportional to τ is dominant in the metallic region, while the interband process is dominant in the insulating region for $n_e=0.5$, 1, and 1.5, although the latter contribution is much smaller compared to the former one; the typical magnitude of the latter contribution is around 10^{-4}.

The magnitude of the linear spin conductivity is maximized for $n_e\sim0.65$ and small $h_{\rm CO}\sim0$. We show the n_e dependence of $\sigma_{xy}^{z({\rm s})}$ at $h_{\rm CO}=0.1$ in Fig. 3(b), where $\sigma_{xy}^{z({\rm s})}$ is also maximized around $n_e\sim0.65$. From the viewpoint of the electronic structure, $\sigma_{xy}^{z({\rm s})}$ tends to be larger when the Fermi level lies on the energy with the high-velocity wave vector in the spin-split band dispersion, as denoted by the horizontal dashed line in Fig. 2(b).

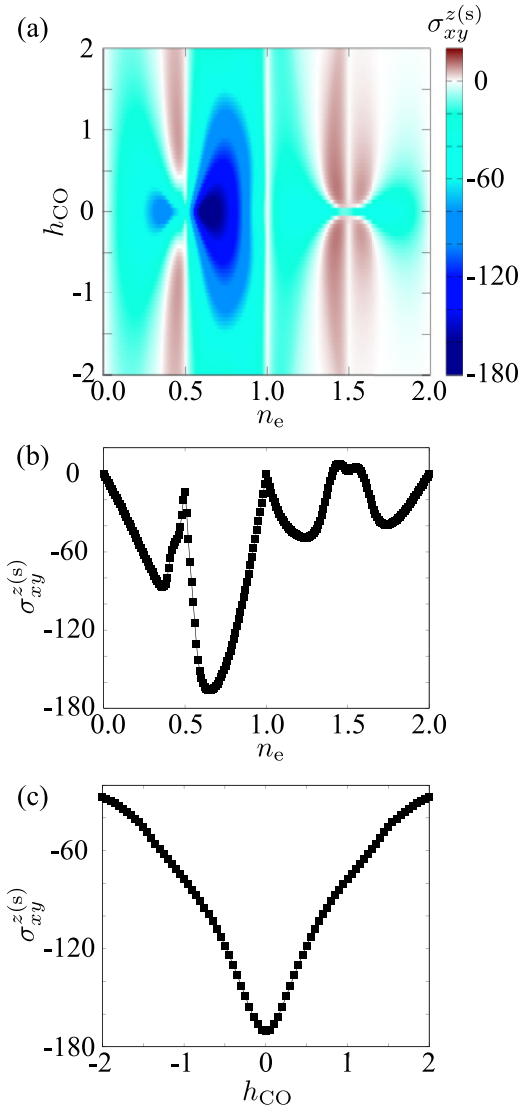

FIG. 3. (a) Contour plots of $\sigma_{xy}^{z({\rm s})}$ in the plane of n_e and $h_{\rm CO}$ at $t_a=1$, $t_b=0.9$, $t_a'=0.3$, $t_b'=0.27$, and $h_{\rm AFM}=3$. It is noted that $\sigma_{xy}^{z({\rm s})}$ values are small but nonzero values in the white region for $0<n_e<2$ owing to the interband process; see the text for details. (b) n_e dependence of $\sigma_{xy}^{z({\rm s})}$ at $h_{\rm CO}=0.1$. (c) $h_{\rm CO}$ dependence of $\sigma_{xy}^{z({\rm s})}$ at $n_e=0.65$.

In addition, one finds that the values of $\sigma_{xy}^{z({\rm s})}$ smoothly change when $h_{\rm CO}$ changes, which indicates that the polar-type symmetry lowering does not affect the linear spin conductivity at the qualitative level. Furthermore, $\sigma_{xy}^{z({\rm s})}$ behaves symmetric in terms of $h_{\rm CO}$, as shown in Fig. 3(c). The suppression of $\sigma_{xy}^{z({\rm s})}$ for larger $h_{\rm CO}$ might be attributed to the fact that $h_{\rm CO}$ tends to localize the electrons in real space, which results in the dispersionless band.

Let us remark on the relationship between $\sigma_{xy}^{z({\rm s})}$ and the symmetric spin-split band structure. As discussed above, $\sigma_{xy}^{z({\rm s})}$

tends to be larger when the spin-split band is more dispersive. Meanwhile, $\sigma_{xy}^{z(\mathrm{s})}$ remains nonzero even when the effect of the diagonal hopping is turned off so as to vanish the symmetric spin splitting. This is owing to the presence of the interband contribution in $\sigma_{xy}^{z(\mathrm{s})}$, although its magnitude is drastically suppressed; for example, the maximum value of $\sigma_{xy}^{z(\mathrm{s})}$ at $h_{\mathrm{CO}} = 0$ and $t_a' = t_b' = 0$ is around the order of 10^{-1} at most.

C. Nonlinear spin conductivity

Next, we investigate the nonlinear spin Hall conductivity $\sigma_{\gamma\mu\nu}^{\eta(\mathrm{s})}$ in Eq. (2), which is evaluated by the second-order Kubo formula with the relaxation time approximation as follows [63,93]:

$$\sigma_{\gamma\mu\nu}^{\eta(\mathrm{s})} = \frac{e^3\tau}{2\hbar^2 N_{\boldsymbol{k}}} \sum_{\boldsymbol{k},n} f_{n\boldsymbol{k}} \epsilon_{\gamma\mu\lambda} D_n^{\nu\lambda(\mathrm{s})}(\boldsymbol{k}) + [\mu \leftrightarrow \nu], \qquad (9)$$

where e, $\hbar$, and $\epsilon_{\eta\mu\lambda}$ represent the electron charge, the reduced Planck constant, and the Levi-Civita tensor, respectively; we take $e = \hbar = 1$. $f_{n\boldsymbol{k}}$ is the Fermi distribution function with the band index n. $D_n^{\mu\nu(\mathrm{s})}(\boldsymbol{k})$ corresponds to the spin-dependent Berry curvature dipole, which is related to the spin-dependent Berry curvature $\Omega_n^{\nu(\mathrm{s})}(\boldsymbol{k})$ as $D_n^{\mu\nu(\mathrm{s})}(\boldsymbol{k}) = \partial_\mu \Omega_n^{\nu(\mathrm{s})}(\boldsymbol{k})$ [93,94]. Since the collinear AFM structure with the z-spin polarization is supposed, $D_n^{\mu\nu(\mathrm{s})}(\boldsymbol{k})$ is expressed as the difference between up-spin and down-spin components like the linear spin Hall conductivity [95]. The nonzero tensor components of $\sigma_{\gamma\mu\nu}^{\eta(\mathrm{s})}$ in the present system satisfy the antisymmetric tensor property in terms of the interchange between γ and $\mu(\nu)$, i.e., $\sigma_{xyy}^{z(\mathrm{s})} = -2\sigma_{yxy}^{z(\mathrm{s})}$; factor 2 arises from the symmetrization regarding the input electric field.

Figure 4(a) shows the contour plot of $\sigma_{xyy}^{z(\mathrm{s})}$ against n_e and h_{CO}. $\sigma_{xyy}^{z(\mathrm{s})}$ becomes nonzero except for $h_{\mathrm{CO}} = 0$, which indicates that the magnetic toroidal dipole induced by nonzero h_{CO} plays an important role. In addition, $\sigma_{xyy}^{z(\mathrm{s})}$ also vanishes for the commensurate electron fillings where the band gap opens, since the expression in Eq. (9) consists of the contribution from both intraband and interband processes. The magnitude of $\sigma_{xyy}^{z(\mathrm{s})}$ is largely enhanced in the region around $n_e \sim 1.5$ and $h_{\mathrm{CO}} \sim 0$, which is much larger than those in the other regions by the order of 10^2–10^3.

We show the n_e dependence of $\sigma_{xyy}^{z(\mathrm{s})}$ at $h_{\mathrm{CO}} = 0.1$ in Fig. 4(b), where $\sigma_{xyy}^{z(\mathrm{s})}$ shows the largest positive and negative values at $n_e \simeq 1.65$ and 1.36, respectively. Such an enhancement of particular electron fillings is understood from the electronic band structure, where the Fermi level corresponding to $n_e = 1.36$ is shown by the horizontal dotted line in Fig. 2(b). One finds that $\sigma_{xyy}^{z(\mathrm{s})}$ is enhanced when the Fermi level is located near the band with a small band gap; the small denominator arising from the small band gap in the expression in Eq. (9) tends to lead to large $\sigma_{xyy}^{z(\mathrm{s})}$.

$\sigma_{xyy}^{z(\mathrm{s})}$ vanishes when setting $t_a = t_b$ and $t_a' = t_b'$. This is because the magnetic toroidal moment in the small square plaquette consisting of t_a and t_a' is canceled out with that in the large square plaquette consisting of t_b and t_b' in such a situation. On the other hand, $\sigma_{xyy}^{z(\mathrm{s})}$ remains nonzero when setting $t_a' = t_b' = 0$. In contrast to the linear spin conductivity $\sigma_{xy}^{z(\mathrm{s})}$, $\sigma_{xyy}^{z(\mathrm{s})}$ exhibits a value similar to that for $t_a', t_b' \neq 0$. In other words, the diagonal hoppings do not affect $\sigma_{xy}^{z(\mathrm{s})}$ at the qualitative level.

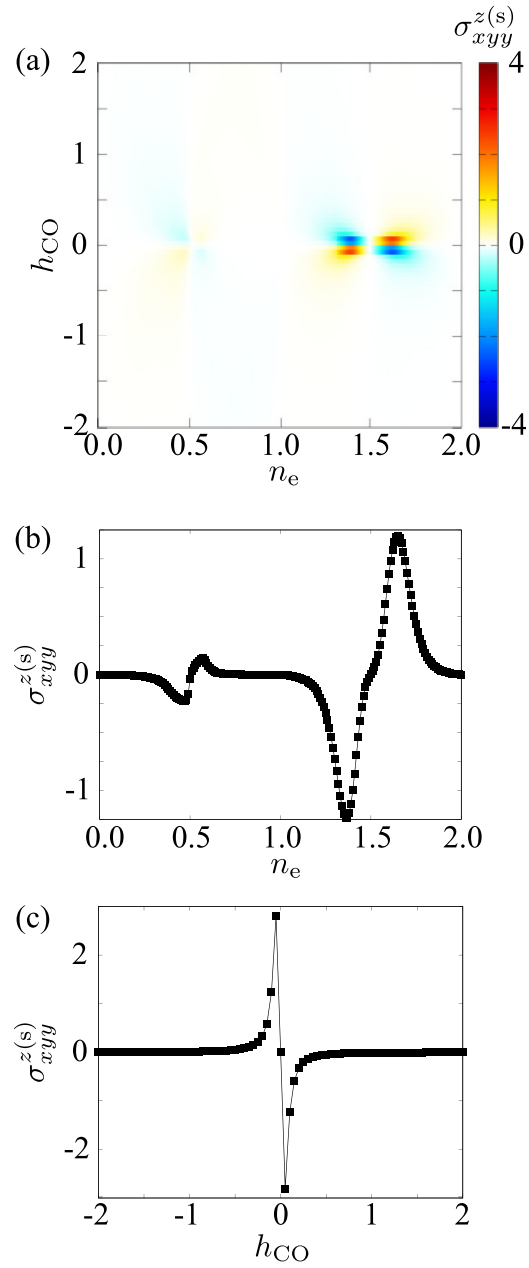

FIG. 4. (a) Contour plots of $\sigma_{xyy}^{z(\mathrm{s})}$ in the plane of n_e and h_{CO} at $t_a = 1$, $t_b = 0.9$, $t_a' = 0.3$, $t_b' = 0.27$, and $h_{\mathrm{AFM}} = 3$. (b) n_e dependence of $\sigma_{xyy}^{z(\mathrm{s})}$ at $h_{\mathrm{CO}} = 0.1$. (c) h_{CO} dependence of $\sigma_{xyy}^{z(\mathrm{s})}$ at $n_e = 1.36$.

V. DISCUSSION

Finally, let us compare the behavior of the linear spin conductivity $\sigma_{xy}^{z(\mathrm{s})} = \sigma_{yx}^{z(\mathrm{s})}$ and the nonlinear spin conductivity $\sigma_{xyy}^{z(\mathrm{s})} = -2\sigma_{yxy}^{z(\mathrm{s})}$. When the system is polar, i.e., $h_{\mathrm{CO}} \neq 0$, both contributions are nonzero in general, and they show the same τ dependence. Meanwhile, their angle dependence is different from each other, which indicates that an experimental signal is different depending on the input electric field direction [26,63]. For example, the linear and nonlinear spin currents

are generated in the x direction when the electric field is applied in the y direction, whereas only the linear spin current is generated in the y direction when the electric field is applied in the x direction. Thus, the measurement of $\sigma_{yx}^{z(s)}$ enables us to extract the pure linear contribution in the spin conductivity tensor. Similarly, one can extract the pure nonlinear contribution by appropriately choosing the input electric field and the output current directions. For example, only the nonlinear spin current is found in the $\langle\bar{1}10\rangle$ direction when the electric field is applied in the $\langle 110\rangle$ direction.

When both linear and nonlinear spin conductivities are nonzero, the magnitude of the linear contribution is much larger than that of the nonlinear contribution, as shown in Figs. 3(a) and 4(a). However, such a situation can be changed depending on the model parameters, since the microscopic origins of the linear and nonlinear spin conductivities are different from each other. For the linear spin conductivity, the symmetric spin-split band structure plays an important role. Since the presence and the absence of the spin splitting depends on the hopping parameters, one might design the system with a large or small linear spin conductivity. For example, the magnitude of the diagonal hopping, which corresponds to the essential ingredient of the spin splitting in the present four-sublattice tetragonal system, determines the magnitude of the linear spin conductivity. Meanwhile, for the nonlinear spin conductivity, the signal is enhanced when the Fermi level is located near the small band gap, while it is not affected by the presence and the absence of diagonal hopping. Thus, one can expect that the contribution from the nonlinear spin conductivity can become larger than that from the linear spin conductivity if the situation satisfies the following two conditions: One is that the hopping contributing to the spin-split band structure is small and the other is that the Fermi level is tuned so as to be located near the small band gap.

VI. SUMMARY

To summarize, we have investigated the effect of the polar-type symmetry lowering in collinear AFMs without the SOC by focusing on the behavior of the linear and nonlinear spin conductivities. Based on the symmetry analysis, we have shown that the linear spin conductivity is induced when the magnetic toroidal quadrupole is activated, while the nonlinear spin conductivity is induced when the magnetic toroidal dipole is activated. Furthermore, we have found the microscopic conditions to enhance the linear and nonlinear spin conductivities by analyzing the fundamental tight-binding model. The symmetric spin-split band structure under the collinear AFM ordering plays an important role in enhancing the linear spin conductivity, while the tuning of the Fermi level is important in enhancing the nonlinear spin conductivity. Finally, we discuss the similarities and the differences between both spin conductivities. Our results can be straightforwardly applied to other lattice structures; once the symmetry of the system under AFMs corresponds to the magnetic point group in Table II, the linear and nonlinear spin conductivities by the same mechanisms are expected. Since the polar-type electric field exists not only in bulk but also at the surface, our results would be beneficial when the thin film system is considered with the application to spintronics devices in mind.

ACKNOWLEDGMENTS

This research was supported by JSPS KAKENHI under Grants No. JP21H01037, No. JP22H04468, No. JP22H00101, No. JP22H01183, No. JP23H04869, No. JP23K03288, and No. JP23K20827; by JST PRESTO (Grant No. JPMJPR20L8); and by JST CREST (Grant No. JPMJCR23O4). Parts of the numerical calculations were performed on the supercomputing systems at the ISSP, the University of Tokyo.

[1] M. Z. Hasan and C. L. Kane, Rev. Mod. Phys. **82**, 3045 (2010).
[2] X.-L. Qi and S.-C. Zhang, Rev. Mod. Phys. **83**, 1057 (2011).
[3] U. K. Rößler, A. N. Bogdanov, and C. Pfleiderer, Nature (London) **442**, 797 (2006).
[4] S. Mühlbauer, B. Binz, F. Jonietz, C. Pfleiderer, A. Rosch, A. Neubauer, R. Georgii, and P. Böni, Science **323**, 915 (2009).
[5] N. Nagaosa and Y. Tokura, Nat. Nanotechnol. **8**, 899 (2013).
[6] J. E. Hirsch, Phys. Rev. Lett. **83**, 1834 (1999).
[7] J. Sinova, D. Culcer, Q. Niu, N. A. Sinitsyn, T. Jungwirth, and A. H. MacDonald, Phys. Rev. Lett. **92**, 126603 (2004).
[8] M. Fiebig, J. Phys. D: Appl. Phys. **38**, R123 (2005).
[9] N. A. Spaldin and M. Fiebig, Science **309**, 391 (2005).
[10] S.-W. Cheong and M. Mostovoy, Nat. Mater. **6**, 13 (2007).
[11] H. Schmid, J. Phys.: Condens. Matter **20**, 434201 (2008).
[12] J. Ye, Y. B. Kim, A. J. Millis, B. I. Shraiman, P. Majumdar, and Z. Tešanović, Phys. Rev. Lett. **83**, 3737 (1999).
[13] T. Jungwirth, Q. Niu, and A. H. MacDonald, Phys. Rev. Lett. **88**, 207208 (2002).
[14] F. D. M. Haldane, Phys. Rev. Lett. **93**, 206602 (2004).
[15] N. Nagaosa, J. Sinova, S. Onoda, A. H. MacDonald, and N. P. Ong, Rev. Mod. Phys. **82**, 1539 (2010).
[16] D. Xiao, M.-C. Chang, and Q. Niu, Rev. Mod. Phys. **82**, 1959 (2010).
[17] G. L. J. A. Rikken, J. Fölling, and P. Wyder, Phys. Rev. Lett. **87**, 236602 (2001).
[18] T. Ideue, K. Hamamoto, S. Koshikawa, M. Ezawa, S. Shimizu, Y. Kaneko, Y. Tokura, N. Nagaosa, and Y. Iwasa, Nat. Phys. **13**, 578 (2017).
[19] Y. Tokura and N. Nagaosa, Nat. Commun. **9**, 3740 (2018).
[20] E. Bauer and M. Sigrist, Editors, *Non-Centrosymmetric Superconductors: Introduction and Overview*, Lecture Notes in Physics (Springer, Berlin, 2012).
[21] S. Yip, Annu. Rev. Condens. Matter Phys. **5**, 15 (2014).
[22] M. Smidman, M. Salamon, H. Yuan, and D. Agterberg, Rep. Prog. Phys. **80**, 036501 (2017).
[23] Y. Noda, K. Ohno, and S. Nakamura, Phys. Chem. Chem. Phys. **18**, 13294 (2016).
[24] T. Okugawa, K. Ohno, Y. Noda, and S. Nakamura, J. Phys.: Condens. Matter **30**, 075502 (2018).
[25] K.-H. Ahn, A. Hariki, K.-W. Lee, and J. Kuneš, Phys. Rev. B **99**, 184432 (2019).

[26] M. Naka, S. Hayami, H. Kusunose, Y. Yanagi, Y. Motome, and H. Seo, Nat. Commun. **10**, 4305 (2019).
[27] S. Hayami, Y. Yanagi, and H. Kusunose, J. Phys. Soc. Jpn. **88**, 123702 (2019).
[28] L.-D. Yuan, Z. Wang, J.-W. Luo, E. I. Rashba, and A. Zunger, Phys. Rev. B **102**, 014422 (2020).
[29] S. Hayami, Y. Yanagi, and H. Kusunose, Phys. Rev. B **102**, 144441 (2020).
[30] M. Naka, Y. Motome, and H. Seo, Phys. Rev. B **103**, 125114 (2021).
[31] D.-F. Shao, S.-H. Zhang, M. Li, C.-B. Eom, and E. Y. Tsymbal, Nat. Commun. **12**, 7061 (2021).
[32] S. A. Egorov and R. A. Evarestov, J. Phys. Chem. Lett. **12**, 2363 (2021).
[33] L.-D. Yuan, Z. Wang, J.-W. Luo, and A. Zunger, Phys. Rev. Mater. **5**, 014409 (2021).
[34] S. Hayami and M. Yatsushiro, J. Phys. Soc. Jpn. **91**, 063702 (2022).
[35] L. Šmejkal, J. Sinova, and T. Jungwirth, Phys. Rev. X **12**, 040501 (2022).
[36] L. Šmejkal, J. Sinova, and T. Jungwirth, Phys. Rev. X **12**, 031042 (2022).
[37] S. W. Lovesey, D. D. Khalyavin, and G. van der Laan, Phys. Rev. B **108**, 174437 (2023).
[38] I. I. Mazin, Phys. Rev. B **107**, L100418 (2023).
[39] L.-D. Yuan and A. Zunger, Adv. Mater. **35**, 2211966 (2023).
[40] L.-D. Yuan, X. Zhang, C. M. Acosta, and A. Zunger, Nat. Commun. **14**, 5301 (2023).
[41] R. D. Gonzalez Betancourt, J. Zubáč, R. Gonzalez-Hernandez, K. Geishendorf, Z. Šobáň, G. Springholz, K. Olejník, L. Šmejkal, J. Sinova, T. Jungwirth *et al.*, Phys. Rev. Lett. **130**, 036702 (2023).
[42] J. A. Ouassou, A. Brataas, and J. Linder, Phys. Rev. Lett. **131**, 076003 (2023).
[43] Q. Cui, B. Zeng, P. Cui, T. Yu, and H. Yang, Phys. Rev. B **108**, L180401 (2023).
[44] B. Brekke, A. Brataas, and A. Sudbø, Phys. Rev. B **108**, 224421 (2023).
[45] T. Osumi, S. Souma, T. Aoyama, K. Yamauchi, A. Honma, K. Nakayama, T. Takahashi, K. Ohgushi, and T. Sato, Phys. Rev. B **109**, 115102 (2024).
[46] A. Hariki, Y. Takahashi, and J. Kuneš, Phys. Rev. B **109**, 094413 (2024).
[47] T. Aoyama and K. Ohgushi, Phys. Rev. Mater. **8**, L041402 (2024).
[48] R. González-Hernández, L. Šmejkal, K. Výborný, Y. Yahagi, J. Sinova, T. Jungwirth, and J. Železný, Phys. Rev. Lett. **126**, 127701 (2021).
[49] H. Bai, Y. C. Zhang, Y. J. Zhou, P. Chen, C. H. Wan, L. Han, W. X. Zhu, S. X. Liang, Y. C. Su, X. F. Han *et al.*, Phys. Rev. Lett. **130**, 216701 (2023).
[50] S. Hayami, M. Yatsushiro, Y. Yanagi, and H. Kusunose, Phys. Rev. B **98**, 165110 (2018).
[51] I. Turek, Phys. Rev. B **106**, 094432 (2022).
[52] P. Liu, J. Li, J. Han, X. Wan, and Q. Liu, Phys. Rev. X **12**, 021016 (2022).
[53] J. Ren, X. Chen, Y. Zhu, Y. Yu, A. Zhang, J. Li, C. Li, and Q. Liu, arXiv:2307.10369.
[54] H. Watanabe, K. Shinohara, T. Nomoto, A. Togo, and R. Arita, Phys. Rev. B **109**, 094438 (2024).
[55] S. A. Egorov, D. B. Litvin, and R. A. Evarestov, J. Phys. Chem. C **125**, 16147 (2021).
[56] S. Hayami, Y. Yanagi, and H. Kusunose, Phys. Rev. B **101**, 220403(R) (2020).
[57] S. Hayami, Phys. Rev. B **105**, 024413 (2022).
[58] S. Hayami, T. Okubo, and Y. Motome, Nat. Commun. **12**, 6927 (2021).
[59] S. Hayami and R. Yambe, Phys. Rev. Res. **3**, 043158 (2021).
[60] S. Hayami and M. Yatsushiro, Phys. Rev. B **106**, 014420 (2022).
[61] S. Hayami and M. Yatsushiro, J. Phys. Soc. Jpn. **91**, 094704 (2022).
[62] R. Eto, R. Pohle, and M. Mochizuki, Phys. Rev. Lett. **129**, 017201 (2022).
[63] S. Hayami, M. Yatsushiro, and H. Kusunose, Phys. Rev. B **106**, 024405 (2022).
[64] M. Yatsushiro, H. Kusunose, and S. Hayami, Phys. Rev. B **104**, 054412 (2021).
[65] Y. Jiang, Z. Song, T. Zhu, Z. Fang, H. Weng, Z.-X. Liu, J. Yang, and C. Fang, arXiv:2307.10371.
[66] Z. Xiao, J. Zhao, Y. Li, R. Shindou, and Z.-D. Song, arXiv:2307.10364.
[67] H. Schiff, A. Corticelli, A. Guerreiro, J. Romhányi, and P. McClarty, arXiv:2307.12784.
[68] M. Seemann, D. Ködderitzsch, S. Wimmer, and H. Ebert, Phys. Rev. B **92**, 155138 (2015).
[69] J. Železný, Y. Zhang, C. Felser, and B. Yan, Phys. Rev. Lett. **119**, 187204 (2017).
[70] A. Mook, R. R. Neumann, A. Johansson, J. Henk, and I. Mertig, Phys. Rev. Res. **2**, 023065 (2020).
[71] S. Hayami and H. Kusunose, J. Phys. Soc. Jpn. **93**, 072001 (2024).
[72] S. Hayami, H. Kusunose, and Y. Motome, J. Phys.: Condens. Matter **28**, 395601 (2016).
[73] M.-T. Suzuki, T. Koretsune, M. Ochi, and R. Arita, Phys. Rev. B **95**, 094406 (2017).
[74] M.-T. Suzuki, H. Ikeda, and P. M. Oppeneer, J. Phys. Soc. Jpn. **87**, 041008 (2018).
[75] M.-T. Suzuki, T. Nomoto, R. Arita, Y. Yanagi, S. Hayami, and H. Kusunose, Phys. Rev. B **99**, 174407 (2019).
[76] H. Yu, Y. Wu, G.-B. Liu, X. Xu, and W. Yao, Phys. Rev. Lett. **113**, 156603 (2014).
[77] K. Hamamoto, M. Ezawa, K. W. Kim, T. Morimoto, and N. Nagaosa, Phys. Rev. B **95**, 224430 (2017).
[78] Y. Araki, Sci. Rep. **8**, 15236 (2018).
[79] A. Pan and D. C. Marinescu, Phys. Rev. B **99**, 245204 (2019).
[80] Z.-F. Zhang, Z.-G. Zhu, and G. Su, Phys. Rev. B **104**, 115140 (2021).
[81] C. Ederer and N. A. Spaldin, Phys. Rev. B **76**, 214404 (2007).
[82] N. A. Spaldin, M. Fiebig, and M. Mostovoy, J. Phys.: Condens. Matter **20**, 434203 (2008).
[83] Y. V. Kopaev, Phys.-Usp. **52**, 1111 (2009).
[84] Y. Yanase, J. Phys. Soc. Jpn. **83**, 014703 (2014).
[85] S. Hayami, H. Kusunose, and Y. Motome, J. Phys. Soc. Jpn. **84**, 064717 (2015).
[86] S. Hayami, H. Kusunose, and Y. Motome, J. Phys. Soc. Jpn. **85**, 053705 (2016).
[87] F. Thöle and N. A. Spaldin, Philos. Trans. R. Soc. A **376**, 20170450 (2018).
[88] Y. Gao, D. Vanderbilt, and D. Xiao, Phys. Rev. B **97**, 134423 (2018).

[89] Y. Gao and D. Xiao, Phys. Rev. B **98**, 060402(R) (2018).
[90] A. Shitade, H. Watanabe, and Y. Yanase, Phys. Rev. B **98**, 020407(R) (2018).
[91] M. Yatsushiro, R. Oiwa, H. Kusunose, and S. Hayami, Phys. Rev. B **105**, 155157 (2022).
[92] A. Kirikoshi and S. Hayami, Phys. Rev. B **107**, 155109 (2023).
[93] I. Sodemann and L. Fu, Phys. Rev. Lett. **115**, 216806 (2015).
[94] H. Kondo and Y. Akagi, Phys. Rev. Res. **4**, 013186 (2022).
[95] C. L. Kane and E. J. Mele, Phys. Rev. Lett. **95**, 226801 (2005).